# Evaluation of Modes in Dielectric Resonators Using a Surface Integral Equation Formulation

ALLEN W. GLISSON, MEMBER, IEEE, DARKO KAJFEZ, SENIOR MEMBER, IEEE, AND JOSEPH JAMES

*Abstract*—**A moment method solution procedure for rotationally symmetric dielectric bodies has been applied to isolated cylindrical dielectric resonators, and the frequencies, as well as $Q$ factors due to radiation, have been determined for several of the lowest modes, including those of hybrid type.**

## I. Introduction

THE ADVANTAGES OF dielectric resonators are their small size, low cost, and good temperature stability. One of the important disadvantages is a proximity of resonant frequencies of various modes. It is therefore of great importance to know the resonant frequency and the field pattern not only for the desired mode of operation (usually $TE_{01\delta}$) but also for other, undesired modes.

Exact field solutions for dielectric resonators are presently available only for the modes with no azimuthal variation (first subscript $m = 0$), and for resonators which conform to a cylindrical system of coordinates [1]–[4]. The higher modes ($m \neq 0$) have been included in a study of scattering from rotationally symmetric bodies by Barber *et al.* [5]. However, their procedure, which employs the extended boundary condition method, has not yet been applied to the study of dielectric resonators.

In this paper, we utilize the method of moments for the analysis of dielectric resonators. The method is applicable for dielectric bodies of revolution with arbitrary cross section and for any azimuthal variation (including hybrid modes with $m \neq 0$). Our approach is based on the solution of a surface integral equation. It offers several computational advantages over finite difference equation or volume integral equation approaches, particularly when the resonator is not enclosed in a metal boundary, such as in the case of isolated resonators.

The experimental determination of resonant frequencies and $Q$ factors of dielectric resonators reported in the literature is restricted to shielded resonators. Shielded resonators have much higher $Q$ values than isolated resonators, and therefore have much more pronounced resonances. However, the resonant frequency of a shielded resonator is modified by the presence of the shielding enclosure. This is even more true with regard to its $Q$ factor. In the present paper, we report on the measurement of resonant frequencies and $Q$ factors of the four lowest modes in dielectric resonators in a free-space environment.

Manuscript received April 7, 1983; revised September 22, 1983. This work was supported in part by the National Science Foundation under Grant ECS-8304442.

The authors are with the Department of Electrical Engineering, University of Mississippi, University, MS 38677.

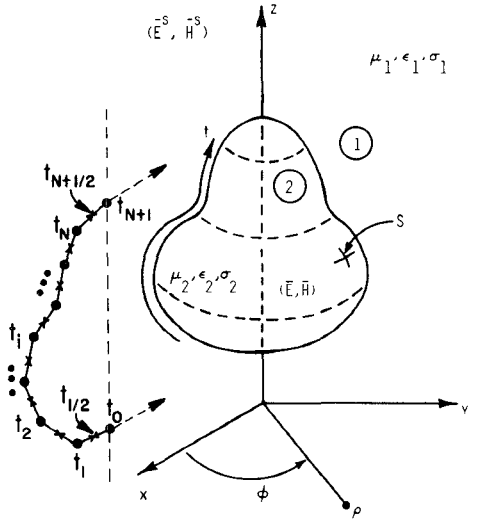


Fig. 1. Geometry and discretization of generating arc for body of revolution.

## II. Surface Integral Equation Formulation

The surface integral equation approach for treating problems involving electromagnetic scattering by dielectric bodies of revolution has been studied by various authors [6]–[9]. In this paper, we adapt the approach presented in [9] to the analysis of rotationally symmetric dielectric resonators. The body of revolution is formed by rotating a planar curve $C$, the so-called generating arc, about an axis which is chosen to be the $z$ axis of a Cartesian coordinate system (Fig. 1). Region 1, exterior to the body, and region 2, interior to the body, are characterized by medium parameters $(\mu_1, \epsilon_1)$ and $(\mu_2, \epsilon_2, \sigma_2)$, respectively. Coordinates $(t, \phi)$ are introduced on the surface $S$, where $t$ is the arc-length along the generating curve and $\phi$ is the azimuthal angle measured from the $x-z$ plane. The orthogonal right-handed triad of unit vectors $(\hat{n}, \hat{\phi}, \hat{t})$ are normal to $S$ and tangent to the $\phi$ and $t$ coordinate lines, respectively. For numerical purposes, the generating arc is approximated as a sequence of linear segments as shown in the figure.

0018-9480/83/1200-1023$01.00 ©1983 IEEE

The exterior fields $(\boldsymbol{E}^s, \boldsymbol{H}^s)$ and the interior fields $(\boldsymbol{E}, \boldsymbol{H})$ may be determined from a set of equivalent electric and magnetic surface currents related to the total tangential surface magnetic and electric fields according to $\boldsymbol{J} = \hat{\boldsymbol{n}} \times \boldsymbol{H}$ and $\boldsymbol{M} = \boldsymbol{E} \times \hat{\boldsymbol{n}}$, respectively. Coupled surface integral equations may be obtained by requiring continuity of the fields tangential to the surface $S$, yielding

$$[\boldsymbol{E}(\boldsymbol{J}, \boldsymbol{M}) + \boldsymbol{E}^s(\boldsymbol{J}, \boldsymbol{M})]_{\tan} = \boldsymbol{0} \tag{1}$$

$$[\boldsymbol{H}(\boldsymbol{J}, \boldsymbol{M}) + \boldsymbol{H}^s(\boldsymbol{J}, \boldsymbol{M})]_{\tan} = \boldsymbol{0} \tag{2}$$

where $(\boldsymbol{E}, \boldsymbol{H})$ and $(\boldsymbol{E}^s, \boldsymbol{H}^s)$ are evaluated just inside and just outside $S$, respectively. The signs preceding all field quantities in (1) and (2) are positive because the correct sources for the interior region are $(-\boldsymbol{J}, -\boldsymbol{M})$ and because the fields are linear, i.e., $-\boldsymbol{E}(-\boldsymbol{J}, -\boldsymbol{M}) = \boldsymbol{E}(\boldsymbol{J}, \boldsymbol{M})$ and $-\boldsymbol{H}(-\boldsymbol{J}, -\boldsymbol{M}) = \boldsymbol{H}(\boldsymbol{J}, \boldsymbol{M})$. The field quantities in (1) and (2) are computed with the aid of homogeneous-region electric and magnetic vector and scalar potentials in which the permittivities and permeabilities used are those appropriate to the region in which the field quantities are evaluated. Equations (1) and (2) are thus expressed as

$$\left\{ j\omega\left[\boldsymbol{A}^1(\boldsymbol{r}) + \boldsymbol{A}^2(\boldsymbol{r})\right] + \nabla\left[\Phi^1(\boldsymbol{r}) + \Phi^2(\boldsymbol{r})\right] + \nabla \times \left[\frac{1}{\epsilon_1}\boldsymbol{F}^1(\boldsymbol{r}) + \frac{1}{\epsilon_2}\boldsymbol{F}^2(\boldsymbol{r})\right]\right\}_{\tan} = \boldsymbol{0} \tag{3}$$

$$\left\{ j\omega\left[\boldsymbol{F}^1(\boldsymbol{r}) + \boldsymbol{F}^2(\boldsymbol{r})\right] + \nabla\left[\Psi^1(\boldsymbol{r}) + \Psi^2(\boldsymbol{r})\right] - \nabla \times \left[\frac{1}{\mu_1}\boldsymbol{A}^1(\boldsymbol{r}) + \frac{1}{\mu_2}\boldsymbol{A}^2(\boldsymbol{r})\right]\right\}_{\tan} = \boldsymbol{0} \tag{4}$$

where the potentials are defined by

$$\boldsymbol{A}^i(\boldsymbol{r}) = \frac{\mu_i}{4\pi}\int_S \boldsymbol{J}(\boldsymbol{r}')G^i(\boldsymbol{r}, \boldsymbol{r}')\, dS' \tag{5}$$

$$\boldsymbol{F}^i(\boldsymbol{r}) = \frac{\epsilon_i}{4\pi}\int_S \boldsymbol{M}(\boldsymbol{r}')G^i(\boldsymbol{r}, \boldsymbol{r}')\, dS' \tag{6}$$

$$\Phi^i(\boldsymbol{r}) = \frac{1}{4\pi\epsilon_i}\int_S \rho^e(\boldsymbol{r}')G^i(\boldsymbol{r}, \boldsymbol{r}')\, dS' \tag{7}$$

$$\Psi^i(\boldsymbol{r}) = \frac{1}{4\pi\mu_i}\int_S \rho^m(\boldsymbol{r}')G^i(\boldsymbol{r}, \boldsymbol{r}')\, dS', \qquad i = 1,2 \tag{8}$$

with

$$G^i(\boldsymbol{r}, \boldsymbol{r}') = \frac{e^{-jk_iR}}{R}, \qquad i = 1,2 \tag{9}$$

$$R = |\boldsymbol{r} - \boldsymbol{r}'| = \left[\rho^2 + \rho'^2 - 2\rho\rho'\cos(\phi - \phi') + (z - z')^2\right]^{1/2}. \tag{10}$$

A time dependence of $\exp(j\omega t)$ is assumed and suppressed. $k_i = \omega\sqrt{\mu_i\epsilon_i}$, $i = 1,2$, is the wavenumber of the associated medium, and $\boldsymbol{r}$ and $\boldsymbol{r}'$ are vectors locating the observation and source coordinates, respectively, in the global coordinate system. Quantities $\rho^e$ and $\rho^m$ appearing in (7) and (8) are the electric and magnetic charge densities which are related to the surface currents through the continuity equations

$$\rho^e(\boldsymbol{r}') = \frac{j}{\omega}\left[\nabla_s' \cdot \boldsymbol{J}(\boldsymbol{r}')\right] \tag{11}$$

$$\rho^m(\boldsymbol{r}') = \frac{j}{\omega}\left[\nabla_s' \cdot \boldsymbol{M}(\boldsymbol{r}')\right]. \tag{12}$$

To take advantage of the rotational symmetry of the body, we expand all currents and scalar Green's functions in Fourier series in $\phi$. For example

$$\boldsymbol{J}(t', \phi') = \sum_{m=-\infty}^{\infty} \boldsymbol{J}_m(t')e^{jm\phi'} \tag{13}$$

$$G^i(t, t', \phi - \phi') = \frac{e^{-jk_iR}}{R} = \frac{1}{2\pi}\sum_{m=-\infty}^{\infty} G_m^i(t, t')e^{jm(\phi - \phi')} \tag{14}$$

where

$$G_m^i(t, t') = \int_{-\pi}^{\pi} G^i(t, t', \alpha)\cos(m\alpha)\, d\alpha. \tag{15}$$

Note that the Fourier expansion of the kernel above is possible because $R = |\boldsymbol{r} - \boldsymbol{r}'|$ is periodic in the variable $(\phi - \phi')$. The magnetic current $\boldsymbol{M}$ is similarly expanded. The Fourier expansion of source and field quantities leads to equations which can be decoupled with respect to the angular variation and subsequently solved for each Fourier component pair $(\boldsymbol{J}_m(t), \boldsymbol{M}_m(t))$ independently.

## III. Numerical Solution

The method of moments is applied to (3) and (4) to obtain for each Fourier component $m$ a set of simultaneous equations which may be represented in matrix form as

$$\underset{\sim}{Z}_m|I_m\rangle = |0\rangle \tag{16}$$

where $\underset{\sim}{Z}_m$ is the moment matrix and $|I_m\rangle$ is a column vector containing the surface current coefficients for the $m$th Fourier component to be determined. To apply the method of moments, the generating arc is approximated as a sequence of linear segments with the discretized $t$ coordinate as shown in Fig. 1. The $t$ variation of each Fourier component of electric current is expanded in the basis functions $\Pi_t^i(t)$ and $\Pi_\phi^i(t)$, where the superscript $i$ now refers to the coordinates $t_i$ rather than the region, as follows:

$$\boldsymbol{J}_m(t) \cong \hat{\boldsymbol{t}}\sum_{i=1}^{N} J_t^{mi}\Pi_t^i(t) + \hat{\boldsymbol{\phi}}\sum_{i=1}^{N+1} J_\phi^{mi}\Pi_\phi^i(t) \tag{17}$$

where

$$\Pi_t^i(t) = \begin{cases} \dfrac{\rho_i}{\rho}, & t_{i-1/2} < t < t_{i+1/2} \\ 0, & \text{otherwise} \end{cases} \tag{18}$$

$$\Pi_\phi^i(t) = \begin{cases} 1, & t_{i-1} < t < t_i \\ 0, & \text{otherwise} \end{cases} \tag{19}$$

The electric charge density is approximated from the continuity equation (11) as

$$\rho_m^e(t) \cong \frac{j}{\omega}\sum_{i=1}^{N+1}\left\{\frac{\rho_i J_t^{mi} - \rho_{i-1}J_t^{m,i-1}}{\rho_{i-1/2}\Delta t_i} + \frac{jm}{\rho_{i-1/2}}J_\phi^{mi}\right\}\Pi^i(t) \tag{20}$$

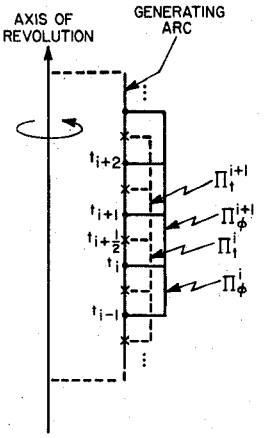


Fig. 2. Interleaved subdomain scheme and basis functions along constant radius portion of generating arc for a cylinder.

where, on the right side of (20), $\rho_\nu = \rho(t_\nu)$, $\Delta t_i = t_i - t_{i-1}$, and $\Pi^i(t) = \Pi_\phi^i(t)$, and where $\rho_0 J_t^{m,0} = \rho_{N+1} J_t^{m,N+1} = 0$. Representations for $\boldsymbol{M}_m$ and $\rho_m^m$ follow from (17) and (20) by replacing electric source quantities by the corresponding magnetic source quantities. Note in (17)–(19) that the two orthogonal current components are interleaved in their spatial representation. This interleaving scheme is illustrated in Fig. 2 for a portion of the generating arc of a cylinder along which the radius is constant (expansion function heights are different for illustration only). The placement of subdomains in this interleaving scheme automatically provides for continuity of the $t$ component of current at body edges (such as on a dielectric cylinder) since the basis function for this component straddles such edges. Basis functions for the $\phi$ component, however, provide for two independent values of the current on either side of a body edge, where this current component may be singular.

Equations (3) and (4) are next tested with the testing functions

$$T_t^{pq}(t,\phi) = \frac{\Pi_t^q(t)}{\rho} e^{-jp\phi} \tag{21}$$

and

$$T_\phi^{pq}(t,\phi) = \frac{\Delta t_q}{\rho} \delta\left(t - t_{q-1/2}\right) e^{-jp\phi}. \tag{22}$$

The $t$ components of (3) and (4) are tested with (21), while the $\phi$ components are tested with (22). The result is a set of simultaneous equations of the form (16) for each Fourier component. Details of the application of the method of moments to obtain (16) are available in [10] and [11].

The matrix equation (16), of course, has a solution only when the determinant of the moment matrix $\underset{\sim}{Z}_m$ is zero:

$$\det\left(\underset{\sim}{Z}_m\right) = 0. \tag{23}$$

The roots of (23) in the complex frequency plane are

$$s_{m,\nu} = \sigma_{m,\nu} + j\omega_{m,\nu} \tag{24}$$

where $\omega_{m,\nu}$ is the resonant frequency of the mode $(m,\nu)$,

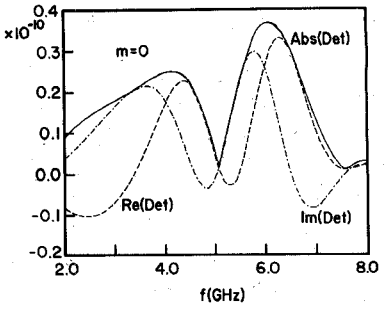


Fig. 3. Moment matrix determinant ($m = 0$) along imaginary axis of complex frequency plane for dielectric cylinder with $\epsilon_r = 35$, $a = 5$ mm, and $h = 5$ mm.

and $\sigma_{m,\nu}$ is inversely proportional to the radiation $Q$ factor

$$Q_{m,\nu} = \frac{\omega_{m,\nu}}{2\sigma_{m,\nu}}. \tag{25}$$

The symbol $\sigma$ used to denote the real part of the complex frequency in (24) and (25) is not to be confused with the conductivity $\sigma$ used in Fig. 1. The search in the complex frequency plane for the roots of (23) can be made fairly efficient for a dielectric resonator because the $Q$ factor for the modes of interest is usually relatively large. Thus it is practical to search along the imaginary axis for crude values of the resonant frequency $\omega_{m,\nu}(2\pi f_{m,\nu})$. A plot of the determinant for $m = 0$ along the imaginary axis of the complex frequency plane is shown in Fig. 3. In this example, the dielectric resonator has $\epsilon_r = 35$, its radius is $a = 5$ mm, and its length is $h = 5$ mm. The absolute value, the real part, and the imaginary part of the determinant are plotted for the Fourier component $m = 0$. The generating arc of the body of revolution is described by 7 points ($N = 5$). As a consequence of the interleaving scheme described above, the resulting matrix is of the size $22 \times 22$. In the range between 2 GHz and 8 GHz the absolute value of the determinant in Fig. 3 shows two distinct minima, one at 5.1 GHz and the other at 7.6 GHz. With the use of diagrams from [4], the two resonant modes can be identified as $TE_{01\delta}$ and $TM_{01\delta}$.

## IV. Determination of Complex Roots

More accurate values of the resonant frequencies as well as the values of the corresponding $Q$ factors can next be determined by extending the search for roots to the complex frequency plane. Fig. 4 shows the behavior of the determinant along a straight line perpendicular to the imaginary axis. It is observed that the absolute value shows a broad minimum, while the real and imaginary parts look almost as two straight lines, each going through zero at a different point. Therefore, the real and imaginary parts of the determinant may each be approximated by a linear function of the complex frequency in the vicinity of the complex root. Using this approximation, it was possible to devise a simple linear search procedure in which each iterative step requires the valuation of the moment matrix at only three points in the complex plane. Since each point is obtained by computing a determinant of a $22 \times 22$ (or larger) matrix, the need for economy of computer time is

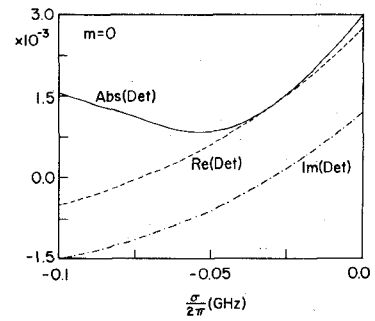


Fig. 4. Example of moment matrix determinant ($m = 0$) along a constant $\omega$ cut in complex frequency plane.

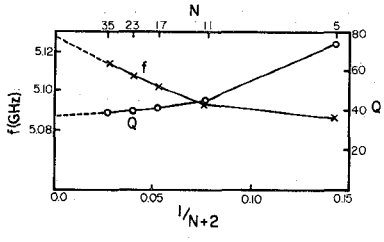


Fig. 5. Convergence plot for frequency and $Q$ factor of dielectric cylinder with $\epsilon_r = 35$, $a = 5$ mm, and $h = 5$ mm.

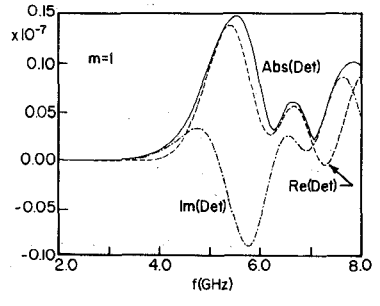


Fig. 6. Moment matrix determinant ($m = 1$) along imaginary axis of complex frequency plane for dielectric cylinder with $\epsilon_r = 35$, $a = 5$ mm, and $h = 5$ mm.

evident. Usually, three to five iterative steps were necessary for an accurate determination of the complex root.

The convergence of the numerical solution was studied by increasing the number of points ($N+2$) on the generating arc from 7 (22 unknowns) to 37 (142 unknowns). The results are plotted versus $1/(N+2)$ in Fig. 5, for the same resonator as before ($\epsilon_r = 35$). One observes that the resonant frequency and the $Q$ factor show good convergence as $N$ is increased. Note that the resonant frequency computed using $N = 5$ differs by less than 1 percent from the extrapolated value of the resonant frequency which would be obtained with an infinite number of points. We take this to be an indication that the computational procedure is well-conditioned. The extrapolated value of resonant frequency for $N \to \infty$ also agrees with [4] within 1 percent while the extrapolated value of $Q$ is lower, coming closer to the values given in [12].

By changing the input parameter from $m = 0$ to $m = 1$, the same computational procedure gives the determinant shown in Fig. 6. The absolute value of the determinant indicates two minima below 8 GHz, one at 6.3 GHz, and another at 7.1 GHz. In accordance with the IEEE standard [13], the hybrid modes on a dielectric resonator are denoted by $\mathrm{HEM}_{mnp}$. The first, second, and third subscripts specify the nature of the azimuthal, radial, and axial variations, respectively. For all the modes encountered in this investigation, the third subscript is smaller than unity, which is denoted by the synbol $\delta$. The two modes visible in Fig. 6 are then tentatively denoted by $\mathrm{HEM}_{11\delta}$ and $\mathrm{HEM}_{12\delta}$.

For a reliable mode identification, it is necessary to compute the detailed field distribution in and around the resonator. In a limited sense, this may be accomplished by studying the distribution of the equivalent surface currents on the resonator, as is done in the next section.

## V. Modal Current Distribution

Once the complex resonant frequency of a mode has been determined to a sufficient degree of accuracy, the modal surface current distributions or, equivalently, the tangential surface fields, can be easily determined. A Gaussian elimination procedure is used to determine the current distributions after the value of one current coefficient is set to some arbitrarily chosen constant. The modal current distributions provide useful guides for determining the mode indices $n$ and $p$ of the particular root found in the complex frequency plane search. (The mode index $m$ is chosen in advance via the testing functions (21) and (22).) The mode indices $n$ and $p$ may be determined more precisely by evaluating the internal fields radiated by the equivalent electric and magnetic currents for the mode.

The examples which follow are computed for a JFD resonator type DRD105UD046, with $\epsilon_r = 38$, $a = 5.25$ mm, and $h = 4.6$ mm. Fig. 7 shows the magnetic surface current $M_t$ (solid line) and the electric surface current $J_\phi$ (dotted line) for the mode $\mathrm{TE}_{01\delta}$. The resonant frequency is 4.829 GHz and the $Q$ factor is 45.8 (for the 18-point model). The horizontal axis in Fig. 7 shows the tangential distance $t$ along the contour of the cylindrical resonator. The vertical axis is the amplitude of the modal surface current (either electric or magnetic) along a constant $\phi$ cut and it has only relative significance, since we investigate the natural response without sources. From the orientation of the surface current such as indicated in Fig. 8, it is seen that $M_t$ is proportional to the $E_\phi$ component of the electric field everywhere on the surface. On the other hand, $J_\phi$ is proportional to $H_\rho$ on each end face of the resonator, and proportional to $H_z$ on the cylindrical surface of length $h$. The straight lines connecting the computed values of the current distribution in Fig. 7, of course, are entirely artificial. Increased resolution of the modal current distribution would require use of a larger value of $N$.

Eighteen points have also been used to evaluate the mode $\mathrm{TM}_{01\delta}$ on the same resonator. The resonant frequency is 7.524 GHz and the $Q$ factor is 76.8. The modal surface currents $J_t$ and $M_\phi$ are shown in Fig. 9.

The hybrid mode $\mathrm{HEM}_{12\delta}$ has the resonant frequency 6.638 GHz and the $Q$ factor 52.1 (evaluated with $N = 25$). The modal currents shown in Figs. 10 and 11, are considerably more complicated, each of them displaying both $t$ and

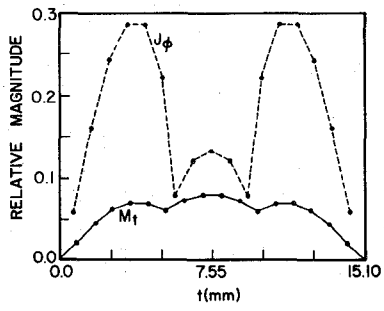


Fig. 7. Magnetic and electric surface current densities for $TE_{01\delta}$ mode on dielectric cylinder with $\epsilon_r = 38$, $a = 5.25$ mm, and $h = 4.6$ mm.

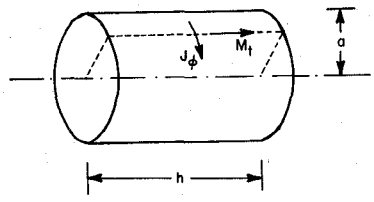


Fig. 8. Surface current orientations on cylindrical dielectric resonator.

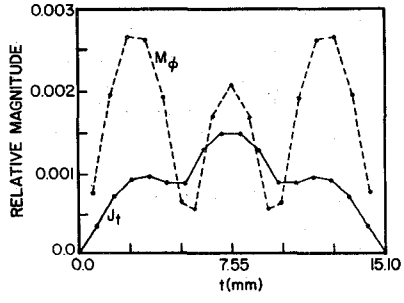


Fig. 9. Magnetic and electric surface current densities for $TM_{01\delta}$ mode on dielectric cylinder with $\epsilon_r = 38$, $a = 5.25$ mm, and $h = 4.6$ mm.

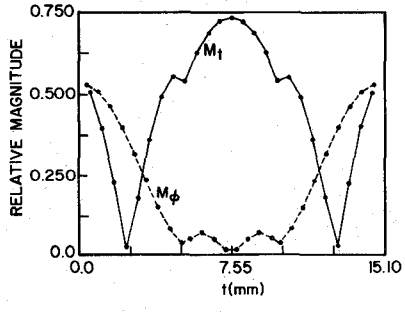


Fig. 10. Magnetic surface current density for $HEM_{12\delta}$ mode on dielectric cylinder with $\epsilon_r = 38$, $a = 5.25$ mm, and $h = 4.6$ mm.

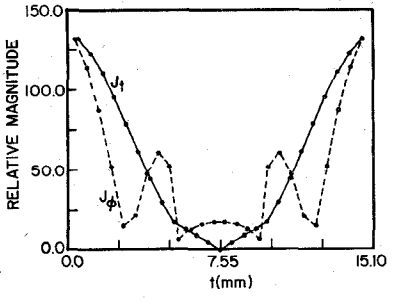


Fig. 11. Electric surface current density for $HEM_{12\delta}$ mode on dielectric cylinder with $\epsilon_r = 38$, $a = 5.25$ mm, and $h = 4.6$ mm.

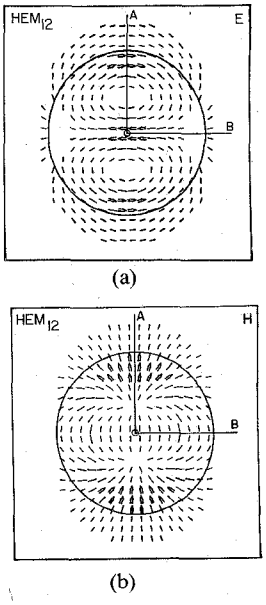


Fig. 12. Waveguide fields of $HEM_{12}$ mode in infinitely long dielectric rod with $\epsilon_r = 38$ and $k_0 a = 0.7299$. (a) Electric field. (b) Magnetic field.

$\phi$ components. The behavior of the modal currents may be better understood when compared with the field patterns in an infinitely long dielectric rod waveguide. The waveguide fields of the mode $HEM_{12}$, generated by computer graphics [14], are shown in Fig. 12. For an observer moving along the line $0A$ in Fig. 12(a), the $E_\phi$ component displays a maximum at the origin. Then, with increasing radius, $E_\phi$ falls to zero and again starts to grow toward a maximum near the outside edge of the dielectric rod. $E_\phi$ is proportional to the surface current $M_t$ which is shown by the solid line in Fig. 10. Indeed, this current indicates a node on each end face of the resonator. The $E_\rho$ component along the line $0A$ in Fig. 12(a) is zero, so that its behavior should be investigated along the line $0B$ instead. The magnitude of the field $E_\rho$ on the end face of the resonator is proportional to $M_\phi$, shown by a dotted line in Fig. 10. In agreement with Fig. 12(a), the magnitude decays with increasing radius approximately to a zero value at the edge of the resonator. A similar qualitative agreement may be established between the magnetic field pattern in Fig. 12(b) and the modal electric surface current shown in Fig. 11.

## VI. Experimental Verification

The experimental verification was performed with a network analyzer, by using the transmission method. The resonator was situated in a box padded with absorbing material. The resonator was coupled to semirigid coaxial cables by a small balanced loop and by a balanced dipole. The balanced arrangement was essential for avoiding external currents on the cable shields, which caused serious difficulties at the beginning of the experimental investigation.

The computed values of the resonant frequencies and $Q$ factors shown in Tables I and II have been obtained with $N = 11$, for the same resonator as before ($\epsilon_r = 38$, $a = 5.25$ mm, $h = 4.6$ mm). The agreement between computed

TABLE I
COMPARISON OF COMPUTED AND MEASURED RESULTS FOR RESONATOR WITH $\epsilon_r = 38$, $a = 5.25$ mm, AND $h = 4.6$ mm
RESONANT FREQUENCY

| MODE | F(GHz) | |
|---|---|---|
| | COMPUTED | MEASURED |
| $TE_{01\delta}$ | 4.82 | 4.85 |
| $HEM_{12\delta}$ | 6.63 | 6.64 |
| $TM_{01\delta}$ | 7.51 | 7.60 |
| $HEM_{21\delta}$ | 7.75 | 7.81 |

TABLE II
COMPARISON OF COMPUTED AND MEASURED RESULTS FOR RESONATOR WITH $\epsilon_r = 38$, $a = 5.25$ mm, AND $h = 4.6$ mm
$Q$ FACTOR

| MODE | Q | | |
|---|---|---|---|
| | COMPUTED | MEASURED (TRANSMISSION METHOD) | MEASURED (REFLECTION METHOD) |
| $TE_{01\delta}$ | 48.5 | 51 | 47 |
| $HEM_{12\delta}$ | 51.9 | 64 | -- |
| $TM_{01\delta}$ | 77.0 | 86 | -- |
| $HEM_{21\delta}$ | 291.0 | 204 | 288 |

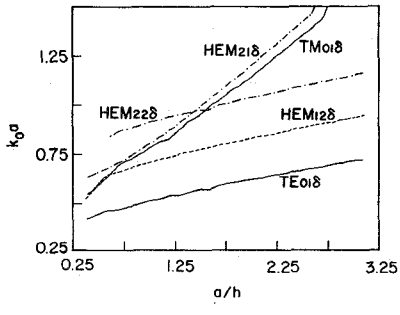


Fig. 13. Universal mode chart for isolated cylindrical dielectric resonators with $\epsilon_r = 38$.

and measured values in resonant frequencies of various modes is about 1 percent, while the disagreement between the computed and measured values of the $Q$ factor is 30 percent in the worst case (mode $HEM_{21\delta}$). As the transmission method is not very reliable for the $Q$ measurement, the reflection method was also attempted. It proved to be difficult to obtain sufficient coupling to the coaxial line, especially for the modes with a low $Q$ factor. For the two modes where the reflection measurement was possible, the agreement in $Q$ was satisfactory (3 percent).

In spite of repeated attempts, it was not possible to observe the resonance of the mode $HEM_{11\delta}$.

## VII. MODE CHART

Encouraged with the experimental verification of the numerical procedure, we computed the universal mode chart for isolated cylindrical dielectric resonators with $\epsilon_r = 38$. The chart is shown in Fig. 13, displaying the value of $k_0 a$ versus the ratio $a/h$. In order to economize the computer time, the resonant frequencies were determined by simply observing the minimum of the determinant on the imaginary axis of the complex plane. The minimum number of points was $N = 11$, but it was necessary to increase it for certain values of $a/h$. Such changes of $N$ have produced slight kinks in the curves shown in Fig. 13.

In this mode chart, the mode $HEM_{11\delta}$ is not shown for two reasons. First, its minimum of the determinant is poorly defined on the imaginary axis, so that it was often overlooked in the search process. Second, the experimental investigation did not demonstrate the existence of this mode.

## VIII. CONCLUSION

A surface integral equation formulation and the method of moments have been applied to the analysis of isolated dielectric resonators. The method has yielded highly accurate values of resonant frequencies and $Q$ factors for both circularly symmetric and hybrid resonator modes. The computational procedure is the same for both types of modes.

The examples described illustrate the power of the formulation used, but they do not exhaust its versatility. The formulation also allows one to model losses in the dielectric material. Lossy dielectrics have not been included here because, in the case of isolated resonators, the dominant losses result from radiation.

Only resonators of cylindrical shape have been studied thus far, whereas the integral equation formulation can be applied to arbitrary rotational bodies by simply modifying the shape of the generating arc. In addition, other rotationally symmetric bodies having the same axis of revolution, such as metal covers, tuning rods, or coupled resonators could be included in the formulation with relative ease. The surface equation formulation presented could also be modified to include simple asymmetric bodies, such as wires, near the resonator [15].

## REFERENCES

[1] Y. Konishi, N. Hosino, and Y. Utsumi, "Resonant frequency of a $TE_{01\delta}$ dielectric resonator," *IEEE Trans. Microwave Theory Tech.*, vol. MTT-24, pp. 112–114, Feb. 1976.

[2] M. Jaworski and M. W. Pospieszalski, "An accurate solution to the cylindrical dielectric resonator problem," *IEEE Trans. Microwave Theory Tech.*, vol. MTT-27, pp. 639–642, July 1979.

[3] P. Guillon, J. P. Balabaud, and Y. Garault, "$TM_{01p}$ tubular and cylindrical dielectric resonator mode," in *IEEE MTT-S Int. Microwave Symp. Dig.*, June 1981, pp. 163–166.

[4] P. Gelin, S. Toutain, P. Kennis, and J. Citerne, "Scattering of the $TE_{01}$ modes on transverse discontinuities in a rod dielectric waveguide—Application to the dielectric resonators," *IEEE Trans. Microwave Theory Tech.*, vol. MTT-29, pp. 712–719, July 1981.

[5] P. W. Barber, J. F. Owen, and R. K. Chang, "Resonant scattering for characterization of axisymmetric dielectric objects," *IEEE Trans. Antennas Propagat.*, vol. AP-30, pp. 168–172, Mar. 1982.

[6] E. N. Vasil'ev and L. B. Materikova, "Excitation of dielectric bodies of revolution," *Sov. Phys.—Tech. Phys.*, vol. 10, pp. 1401–1406, 1966.

[7] T. K. Wu and L. L. Tsai, "Scattering from arbitrarily-shaped lossy dielectric bodies of revolution," *Radio Sci.*, vol. 12, no. 5, pp. 709–718, Sept. 1977.

[8] J. R. Mautz and R. F. Harrington, "Electromagnetic scattering from a homogeneous material body of revolution," *Arch. Elek. Übertragung*, vol. 33, no. 2, pp. 71–80, Feb. 1979.

[9] A. W. Glisson and D. R. Wilton, "Simple and efficient numerical methods for problems of electromagnetic radiation and scattering

from surfaces," *IEEE Trans. Antennas Propagat.*, vol. AP-28, no. 5, pp. 593–603, Sept. 1980.
[10] A. W. Glisson and D. R. Wilton, "Electromagnetic scattering by bodies of revolution," in *Applications of the Method of Moments to Electromagnetic Fields*, B. J. Strait, Ed. Orlando: SCEEE Press, 1980.
[11] A. W. Glisson, "On the development of numerical techniques for treating arbitrarily-shaped surfaces," Ph.D. dissertation, Univ. of Mississippi, University, MS, June 1978.
[12] M. Verplanken and J. Van Bladel, "The electric dipole resonances of ring resonators of very high permittivity," *IEEE Trans. Microwave Theory Tech.*, vol. MTT-24, pp. 108–112, Feb. 1976.
[13] "IRE standards on antennas and waveguides: Definitions of terms, 1953," *Proc. IRE*, vol. 41, pp. 1721–1728, Dec. 1953.
[14] D. Kajfez, "Modal field patterns in dielectric rod waveguide," *Microwave J.*, vol. 26, pp. 181–192, May 1983.
[15] A. W. Glisson and C. M. Butler, "Analysis of a wire antenna in the presence of a body of revolution," *IEEE Trans. Antennas Propagat.*, vol. AP-28, no. 5, pp. 604–609, Sept. 1980.

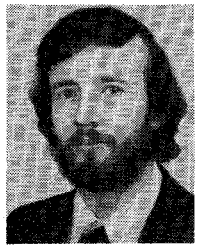

**Allen W. Glisson** (S'71–M'78) was born in Meridian, MS, on June 26, 1951. He received the B.S., M.S., and Ph.D. degrees in electrical engineering from the University of Mississippi, in 1973, 1975, and 1978, respectively.

From 1973 to 1978, he served as a Research Assistant in the Electrical Engineering Department of the University of Mississippi. In 1978, he joined the faculty of the University of Mississippi, where he is currently Assistant Professor of Electrical Engineering. His current research interests include the development and application of numerical techniques for treating electromagnetic radiation and scattering problems.

Dr. Glisson is a member of Sigma Xi, Tau Beta Pi, Phi Kappa Phi, Eta Kappa Nu, and an associate member of Commission B of the International Union of Radio Science.

**Darko Kajfez** (SM'67) received the Dipl. Ing. degree in electrical engineering from the University of Ljubljana, Yugoslavia, in 1953, and the Ph.D. degree from the University of California, Berkeley, in 1967.

Between 1950 and 1963, he was a Research Engineer with companies "Iskra" and "Rudi Cajavec" in Yugoslavia, designing various microwave equipment. In 1967, he joined the University of Mississippi, where he is now a Professor of Electrical Engineering. His research interest is in microwave circuits.

**Joseph James** was born in Chenappady, India, on May 25, 1956. He received the B.S. degree in electronics and communication engineering from the University of Kerala in 1977.

From 1978 to 1981, he worked as a Research Engineer with the Electronics Corporation of India Limited, Hyderabad. He is currently a graduate student in the Department of Electrical Engineering at the University of Mississippi, where he is also employed as a Research Assistant.